ACS APPLIED ENERGY MATERIALS
Cite This: ACS Appl. Energy Mater. XXXX, XXX, XXX−XXX
Letter
www.acsaem.org

Three-Dimensional Visualization of Conductive Domains in Battery Electrodes with Contrast-Enhancing Nanoparticles

Samantha L. Morelly,[†] Jeff Gelb,[‡] Francesco Iacoviello,[§] Paul R. Shearing,[§] Stephen J. Harris,[∥] Nicolas J. Alvarez,[†] and Maureen H. Tang*[,†]

[†]Department of Chemical and Biological Engineering, Drexel University, Philadelphia, Pennsylvania 19104, United States
[‡]Sigray, Incorporated, 5750 Imhoff Drive, Suite I, Concord, California 94520, United States
[§]Electrochemical Innovation Lab, Department of Chemical Engineering, University College London, London WC1E 7JE, United Kingdom
[∥]Materials Science Division, Lawrence Berkeley National Laboratory, Berkeley, California 94720, United States

Supporting Information

ABSTRACT: Replacing conductive carbon black with commercial carbon-coated iron nanoparticles yields an effective contrast-enhancing agent to differentiate between active material, conductive additive, and binder in lithium-ion battery electrodes. Nano-XCT resolved the carbon−binder domain with 126 nm voxel resolution, showing partial coatings around the active material particles and interparticle bridges. In a complementary analysis, SEM/EDS determined individual distributions of conductive additives and binder. Surprisingly, the contrast-enhancing agents showed that the effect of preparation parameters on the heterogeneity of conductive additives was weaker than on the binder. Incorporation of such contrast-enhancing additives can improve understanding of processing−structure−function relationships in a multitude of devices for energy conversion and storage.

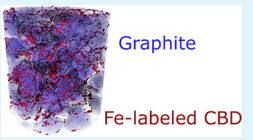

KEYWORDS: *Li-ion battery, battery electrodes, electrode processing, X-ray tomography, nano-CT, heterogeneity*

The ever-increasing demands of power and energy for automotive and consumer product applications require optimal design of battery electrodes. Of major concern in battery design is the carbon−binder domain (CBD) of conductive carbon additives and polymer binder. Although the CBD makes up only a small fraction of electrode mass and volume (typically 3−6 wt % in commercial formulations, but much higher in academic settings), its microstructure has a critical influence on battery performance. Insufficient connectivity of the CBD leads to poor electron transport and insufficient mechanical strength, while excessive CBD adds dead weight and volume at the cell level and may even slow ion transport. Continuum-scale battery performance models do not explicitly consider the CBD and instead predict discharge curves based on effective parameters such as long-range electron conductivity (solid phase), long-range ion tortuosity (liquid phase), and short-range contact resistances (solid phase). The fundamental relationships between CBD microstructure and these transport parameters are currently very poorly understood, as evidenced by the trial-and-error approach to electrode processing optimization.

A major cause for poor understanding of the relationships between processing, microstructure, and performance is the inability to adequately visualize the location and distribution of carbon and binder inside battery electrodes. Scanning electron microscopy coupled with energy dispersive X-ray spectroscopy (SEM/EDS) is currently the most reliable method for visualizing carbon in electrodes.[1−6] Infiltrating electrode voids with a silicon-based resin provides the needed contrast between porosity and CBD regions.[1] Combining SEM with focused ion beam (FIB) milling can obtain 3D reconstructions, but the reconstructions are valid only if the resin does not expand or contract upon hardening, which would alter the microstructure in unknown ways. Furthermore, the cost and time of FIB/SEM is considerable, and the field of view is generally very small. Accordingly, many studies have been devoted to higher throughput methods of electrode imaging based on X-ray computed tomography (XCT).[7−12] High-resolution nano-XCT can image electrodes with resolution as small as 50 nm, while laboratory-scale tomography can commonly resolve images of entire electrodes with resolution of 100−600 nm. However, XCT is fundamentally limited in distinguishing between active material and CBD. If high-energy X-rays are chosen for optimal imaging of a transition metal oxide, the CBD and porosity (voids) appear equally transparent. If low-energy X-rays are chosen for a carbonaceous active material, then low X-ray penetration levels prohibit the study of realistically sized specimens. Continuing efforts to avoid this problem combine XCT with FIB/SEM and image-matching,[10] statistical pore-filling models of the CBD,[11] or separate tomograms in Zernike phase-contrast mode.[12]

In addition to the described limitations, neither XCT nor SEM/EDS is able to separately resolve carbonaceous active materials from conductive carbon. In this work, we present an

Received: July 20, 2018
Accepted: September 5, 2018
Published: September 5, 2018

DOI: 10.1021/acsaem.8b01184
ACS Appl. Energy Mater. XXXX, XXX, XXX−XXX

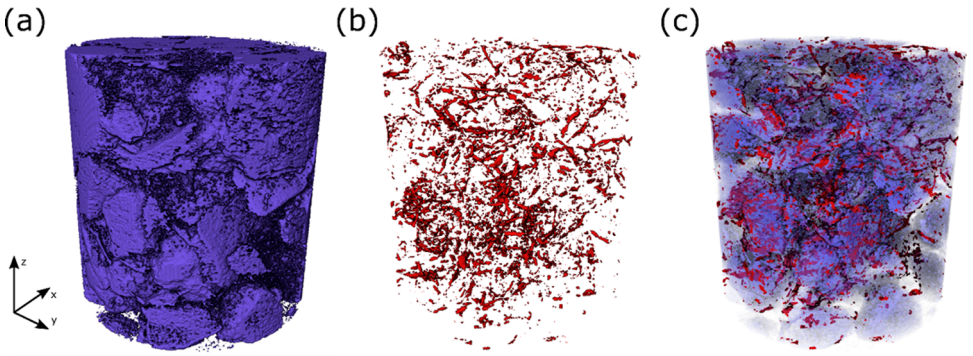

Figure 1. 3D renderings from XCT images of (a) graphite phase, (b) Fe-labeled CBD phase, and (c) both phases with graphite transparency of 1%. The voxel size is 126 nm, and the imaged cylinder is 65 μm in diameter.

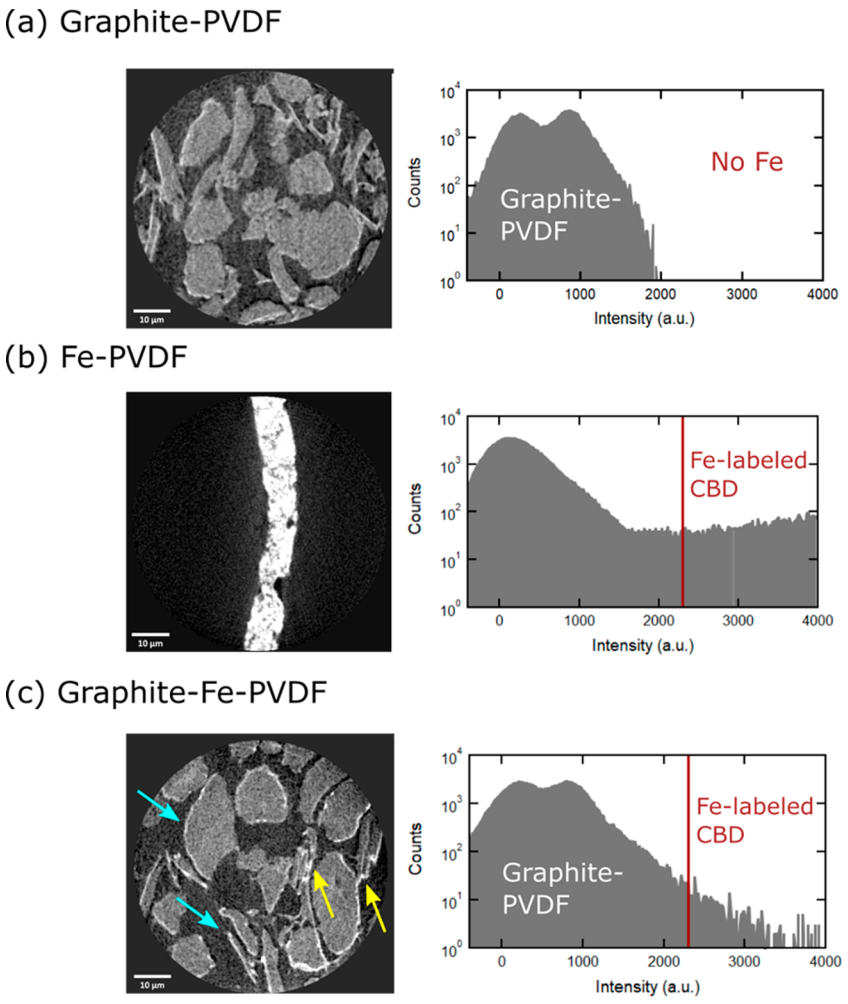

Figure 2. Virtual slices of 3D XCT volume with accompanying histograms for (a) graphite-PVDF, (b) Fe-PVDF, and (c) graphite-Fe-PVDF. The red line indicates the assigned CBD threshold of 2300 (for details, see Supporting Information). Blue and yellow arrows in panel c indicate CBD coatings and bridges between particles, respectively.

innovative solution to these problems by replacing conductive carbon with C-coated Fe nanoparticles (Fe−C). Fe absorbs X-rays hundreds of times more strongly than C or F, thereby enhancing the contrast of the CBD with XCT. In SEM/EDS, the Fe provides a strong signal that differentiates conductive carbon from active materials to determine the homogeneity of the CBD.

As shown in Figure 1, commercial Fe−C nanoparticles were demonstrated as contrast-enhancing agents for XCT by preparing and imaging thin electrodes of Fe-PVDF, graphite-PVDF, and graphite-Fe-PVDF according to literature methods.[13−16] With a diameter of 25 nm, the particle size is very similar to conventional conductive carbon nanoparticles. The carbon coating around the Fe additionally provides a surface chemically similar to conventional conductive carbon.

DOI: 10.1021/acsaem.8b01184
ACS Appl. Energy Mater. XXXX, XXX, XXX−XXX

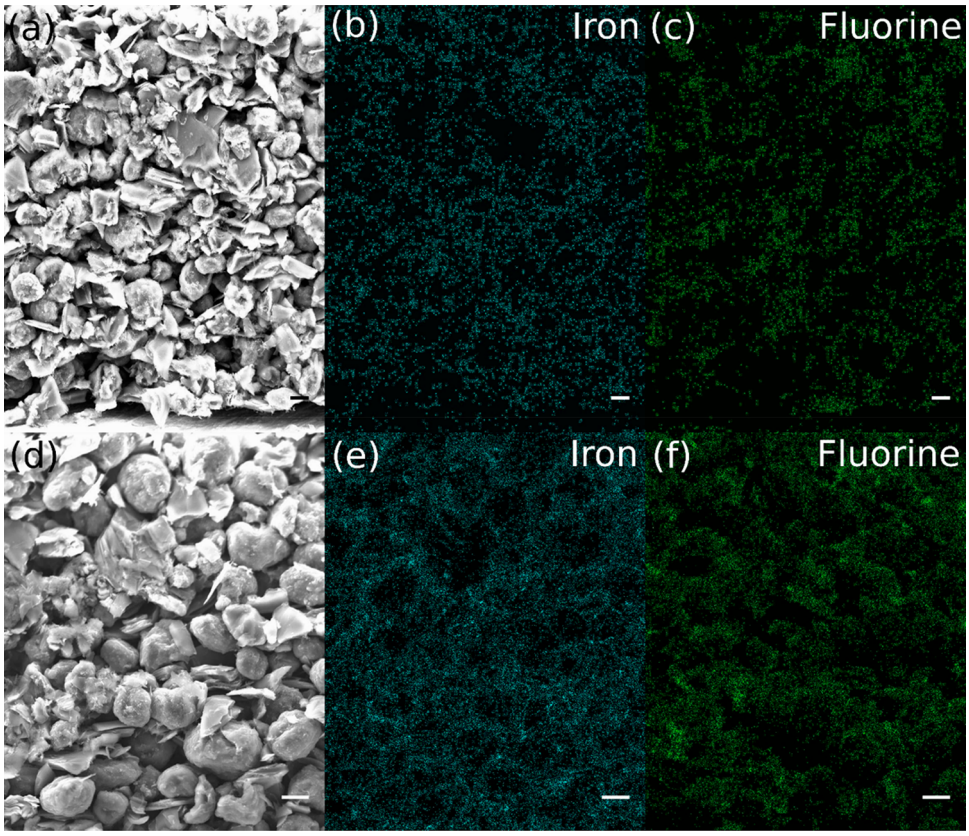

Figure 3. SEM and EDS maps for homogeneously (a−c) and heterogeneously (d−f) prepared graphite electrodes with Fe contrast-enhancing agent. For each image, the current collector appears at the bottom, and the scale bar corresponds to 10 μm. (a, d) SEM images, (b, e) Fe EDS map in cyan, and (c, f) F EDS map in green. For the homogeneously prepared electrode, the Fe and F maps are almost indistinguishable and show a well-dispersed CBD. For the heterogeneously prepared electrode, Fe and F maps show different regions of deficiency, with stronger F enrichment at the electrode surface.

Supporting Information Figure S1 demonstrates the ability of the Fe−C nanoparticles to perform in a functional graphite electrode. All three electrodes were imaged using identical exposure parameters and reconstructed using consistent bounds, which allowed a direct comparison of CT numbers between data sets. Virtual slices of the 3D XCT volume for each of the three electrode samples are accompanied by histograms of voxel intensity in Figure 2. Each data set was reconstructed using the full 32-bit computational dynamic range available in the reconstruction software, in order to avoid CT number (or radiodensity) scaling issues imposed by downsampling to lower bit depths. As such, all reconstruction values were accepted, including the negative values resulting from small amounts of noise in the X-ray radiographs.

Comparison of Figure 2a,b shows that, as expected, graphite-PVDF (a) is much less bright than Fe-PVDF (b). A visual binarization of the Fe-PVDF data set provided a clear means of determining the cutoff threshold value between Fe and PVDF of ∼2300, as shown in Figure 2b. This cutoff was then verified in the graphite-PVDF case (Figure 2a), which registered a negligible number of CT values above 2300 and, thus, confirmed that 2300 was an appropriate Fe threshold. A similar procedure was performed for the graphite-PVDF case in order to set a threshold value for graphite vs PVDF. The resulting final threshold values for PVDF, graphite, and Fe were applied to the graphite-Fe-PVDF case (Figure 2c). These images therefore indicate that the bright spots in panel c surrounding the larger graphite particles represent Fe−C nanoparticles coating the active material surface. In contrast, some brightness can be observed on the edges of the graphite particles in panel a, but the quantitative gray-scale values are far below the Fe thresholds indicated by the Fe-PVDF (b) or graphite-Fe-PVDF (c) intensities.

The virtual slices of the graphite-Fe-PVDF electrode were rendered into 3D images as shown in Figure 1. The 3D rendering of the graphite-PVDF film is shown in Figure S1. Panel a of Figure 1 illustrates the microstructure of the graphite phase, panel b illustrates the microstructure of Fe-labeled CBD, and panel c overlays the graphite and CBD phases. The calculated volume percent of Fe−C is 1.2%, while the volume percent of Fe−C nanoparticles based on the electrode composition is 0.7%. However, the expected volume percent of CBD is 3.9%, assuming homogeneous distribution of Fe−C within the CBD. The missing CBD is attributed to the resolution of the XCT. With a voxel size of 126 nm and a particle diameter of 25 nm, voxels will be detected as pure Fe only if particles are densely packed in clusters of more than 100 particles. Fe−C particles that have been diluted by binder or void will absorb with lower intensity. At sufficiently high dilution, the Fe-PVDF phase will be detected indistinguishably from graphite. Higher resolution imaging would therefore increase the fraction of Fe registered and yield unambiguous structures of the CBD, but at the cost of a smaller field of view and less statistical power.

From Figures 1 and 2, contrast-enhanced XCT clearly affords the specific spatial variations of active material,

DOI: 10.1021/acsaem.8b01184
ACS Appl. Energy Mater. XXXX, XXX, XXX−XXX

Table 1. Volume Fractions of Graphite, CBD, and Void on Entire Sample Volume as Well as Selected Subvolumes with *z*-Direction Connectivity

	entire image	subvolume A	subvolume B	subvolume C
volume (voxels)		60 × 90 × 35	60 × 90 × 35	160 × 160 × 505
volume fraction (vol %)				
graphite	44.9	63.6	48.9	54.7
CBD	1.7	1.7	2.9	0.6
void	53.7	34.7	48.2	44.7
connectivity (%)				
graphite		~100	99	~100
CBD		86	85	0
void		99	94	99

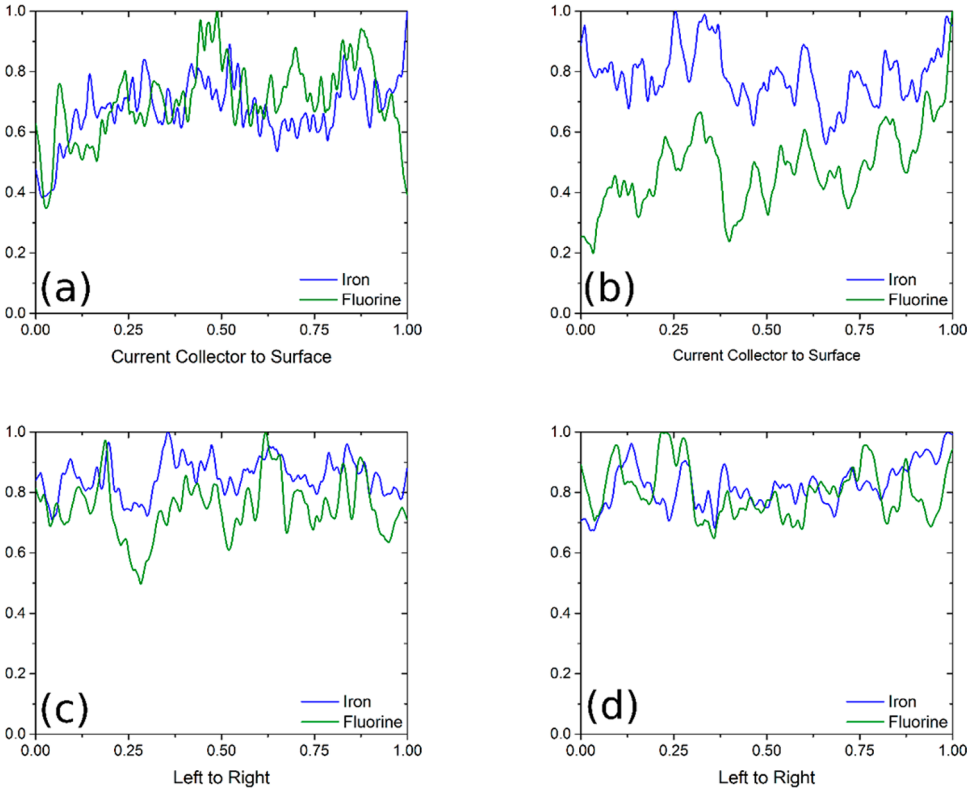

Figure 4. Normalized integrated intensity vs position for (a) homogeneously prepared electrodes, bottom−top; (b) heterogeneously prepared electrodes, bottom−top; (c) homogeneously prepared electrodes, left−right; and (d) heterogeneously prepared electrodes, left−right. Intensities were normalized by the maximum line-integral value for each elemental map.

conductive additive, and void space. From this information, the interconnectivity of conductive additive, void, and graphite can be calculated to provide critical inputs for detailed electrochemical models that predict effective ion and electron transport properties[17] as well as mechanical and thermal behavior.[18] For example, finding the fraction of voxels that share common vertices yields the lower bound percolation ratios, or connectivities, of graphite, void, and conductive additive. Performing this calculation on a selected subvolume (Figure S3) yields a percolation ratio of 100% for graphite, 85% for the CBD, and 99% for voids. The complete connectivity of graphite is predictable, as particles cannot be standing in free space, while the 99% connectivity between voids (which are filled with electrolyte during battery operation) suggests the absence of isolated pockets, which would be unable to transport ions.

The methods presented here can be used to relate processing conditions to electrode microstructure, which in turn influences performance. For example, some recent efforts to model charge transport and mechanical deformation in battery electrodes have considered the effects of CBD present as conformal coatings around active material particles vs "binder bridges" between particles.[19] Figures 1 and 3 show the clear presence of such bridges between particles (indicated by yellow arrows), and the subvolume in Figure S3 shows that they are generally connected. For the entire sample volume imaged, the computed surface area of graphite is 0.19 mm^2, while the surface area of CBD is 0.025 mm^2. The surface area of contacts between graphite and CBD is 0.012 mm^2, showing that CBD bridges between particles cover approximately 6% of the graphite surface. The fraction of surface area covered by CBD bridges will certainly affect particle−particle resistances, which are critical to electrode performance for a variety of systems.[14,20−22]

While bridges between particles are clearly visible from Figures 1 and S3, Figure 2c also appears to show conformal

DOI: 10.1021/acsaem.8b01184
ACS Appl. Energy Mater. XXXX, XXX, XXX−XXX

CBD coatings around some of the graphite particles (blue arrows). However, for 20 μm graphite particles, conformal coating of 3.9 vol % CBD around each particle would yield a thickness of approximately 140 nm. With a voxel size of 126 nm, 140 nm features are smaller than the spatial resolution of the XCT images, as convention suggests that a minimum of two voxels are needed in order to clearly resolve a feature.[23] Considering that much of the CBD is already present as large clusters in the bridges, the actual volume fraction of CBD present as a conformal coating is even less than 3.9 vol %. Thus, thin coatings cannot be visualized without higher resolution XCT.

A major advantage of the contrast-enhancing nanoparticles is the ability to determine the influences of electrode heterogeneity[24] on the distribution of CBD. Table 1 shows that the CBD volume is slightly higher in the subvolume of Figure S3 than in the overall volume, demonstrating mesoscale heterogeneities. The mesoscale heterogeneity is confirmed by completing a similar analysis on varying subvolumes in the electrode, the results of which are shown in Table 1. Because the CBD is the most dilute component, variation in volume fraction leads to the greatest variation in connectivity.

While the results of Table 1 demonstrate the local heterogeneities of CBD distribution, Figure 1b shows that the electrode preparation technique yields Fe−C that is distributed uniformly throughout the macroscopic structure, as evidenced by the homogeneous distribution of bright voxels (>2300) throughout the specimen volume. A homogeneous distribution of Fe−C within the CBD is also supported by the EDS of Figure S4. Thus, contrast-enhanced XCT can be used to determine both microscopic and macroscopic distributions of CBD and active material, if it is demonstrated that the nanoparticles are uniformly distributed in the CBD.

If electrode processing parameters are not chosen correctly, the CBD itself can be inhomogeneous. The contrast-enhancing nanoparticles can also be used to determine this homogeneity, by separately determining binder and conductive additive distributions through SEM/EDS. Thick electrodes (100 μm dry) were chosen to amplify gradients formed during coating and drying.[25] Images are shown in Figure 3. In both images, the SEM shows graphite particles with particle sizes ranging from 20 to 50 μm, consistent with manufacturer specifications. Both the Fe and F maps show the presence of CBD. For the homogeneous electrode, Fe and F show considerable overlap, while the heterogeneous electrode shows enhanced F content close to the electrode surface. Such binder migration to the electrode surface has been well-documented and may be caused when concentration gradients formed by capillary forces during drying have insufficient time to relax.[26−29] The Fe gradient appears less obviously than the strong F gradient, indicating that *homogeneity of the contrast-enhancing agent does not ensure homogeneity of the CBD*.

The heterogeneity of the electrodes in Figure 3 can be analyzed via line integrals of EDS intensity, as shown in Figure 4. Integration of the EDS signal from left to right as shown in Figure 4a shows that, for the homogeneous electrode, neither F nor Fe show an obvious trend from current collector to surface. Figure 4b shows that, for the heterogeneous electrode, the surface F concentration is approximately four times greater than that at the current collector, but the Fe concentration is approximately the same at the current collector and the electrode surface. Integrating the SEMs from top to bottom as shown in Figure 4c,d shows that the oscillations in Fe and F roughly track each other for both electrodes, likely because of variation in local porosity. The combined F/Fe integral scans show that, depending on how the electrode is processed, the CBD may be either homogeneous or heterogeneous on a macroscopic length scale and that conductive additive and binder are independently influenced by processing conditions.

In summary, we have developed a simple, low-cost method to incorporate Fe nanoparticles into battery electrodes as contrast-enhancing agents and have demonstrated their ability to improve visualization of the CBD in both XCT and SEM/EDS. XCT rapidly yields detailed 3D microstructures of the phases, while SEM/EDS provides higher spatial resolution and chemical specificity with widely available instrumentation. Neither method requires synchrotron access, and the two techniques are in fact strongly complementary if SEM/EDS is used to verify homogeneous mixing of the CBD before imaging samples in XCT. These techniques are not limited to Li-ion chemistries; carbonaceous or other low-Z materials are also relevant to beyond-Li systems such as Na-ion, Li− and Na−S, pseudocapacitors, and multivalent intercalation chemistries. Even in fuel cells, researchers must consider how the mesoscale structure of Nafion binder and carbon nanoparticles affect oxygen transport in the catalyst layer. This work presents a simple method to determine the microstructure of active material, conductive additive, and binder that is easily generalizable to a great many of these systems. Efforts to quantify specific microstructures and relate them to electrode lifetime and performance are ongoing.

■ ASSOCIATED CONTENT

Supporting Information

The Supporting Information is available free of charge on the ACS Publications website at DOI: 10.1021/acsaem.8b01184.

Materials and methods, electrode formulations, battery discharge profiles, and additional XCT and SEM/EDS images (PDF)

■ AUTHOR INFORMATION

Corresponding Author

*E-mail: mhtang@drexel.edu.

ORCID

Paul R. Shearing: 0000-0002-1387-9531

Maureen H. Tang: 0000-0003-0037-4814

Notes

The authors declare no competing financial interest.

■ ACKNOWLEDGMENTS

Funding from Drexel University's College of Engineering and from Grant NSF-CBET-1751553 is gratefully acknowledged. S.J.H. acknowledges support from the Assistant Secretary for Energy Efficiency, Vehicle Technologies Office of the U.S. Department of Energy (U.S. DOE) under the Advanced Battery Materials Research (BMR) Program. P.R.S. acknowledges funding from the Royal Academy of Engineering.

■ REFERENCES

(1) Ender, M.; Joos, J.; Carraro, T.; Ivers-Tiffée, E. Three-Dimensional Reconstruction of a Composite Cathode for Lithium-Ion Cells. *Electrochem. Commun.* **2011**, *13*, 166−168.

(2) Wilson, J. R.; Cronin, J. S.; Barnett, S. A.; Harris, S. J. Measurement of Three-Dimensional Microstructure in a LiCoO2 Positive Electrode. *J. Power Sources* **2011**, *196*, 3443−3447.

DOI: 10.1021/acsaem.8b01184
ACS Appl. Energy Mater. XXXX, XXX, XXX−XXX

(3) Hutzenlaub, T.; Thiele, S.; Zengerle, R.; Ziegler, C. Three-Dimensional Reconstruction of a LiCoO2 Li-Ion Battery Cathode. *Electrochem. Solid-State Lett.* **2012**, *15*, A33.
(4) Liu, Z.; Cronin, J. S.; Chen-Wiegart, Y. K.; Wilson, J. R.; Yakal-Kremski, K. J.; Wang, J.; Faber, K. T.; Barnett, S. a. Three-Dimensional Morphological Measurements of LiCoO2 and LiCoO2/Li(Ni1/3Mn1/3Co1/3)O2 Lithium-Ion Battery Cathodes. *J. Power Sources* **2013**, *227*, 267−274.
(5) Hutzenlaub, T.; Thiele, S.; Paust, N.; Spotnitz, R.; Zengerle, R.; Walchshofer, C. Three-Dimensional Electrochemical Li-Ion Battery Modelling Featuring a Focused Ion-Beam/scanning Electron Microscopy Based Three-Phase Reconstruction of a LiCoO2 Cathode. *Electrochim. Acta* **2014**, *115*, 131−139.
(6) Li, Y.; Meyer, S.; Lim, J.; Lee, S. C.; Gent, W. E.; Marchesini, S.; Krishnan, H.; Tyliszczak, T.; Shapiro, D.; Kilcoyne, A. L. D.; Chueh, W. C. Effects of Particle Size, Electronic Connectivity, and Incoherent Nanoscale Domains on the Sequence of Lithiation in LiFePO4 Porous Electrodes. *Adv. Mater.* **2015**, *27*, 6591−6597.
(7) Shearing, P. R.; Howard, L. E.; Jørgensen, P. S.; Brandon, N. P.; Harris, S. J. Characterization of the 3-Dimensional Microstructure of a Graphite Negative Electrode from a Li-Ion Battery. *Electrochem. Commun.* **2010**, *12*, 374−377.
(8) Shearing, P. R.; Brandon, N. P.; Gelb, J.; Bradley, R.; Withers, P. J.; Marquis, A. J.; Cooper, S.; Harris, S. J. Multi Length Scale Microstructural Investigations of a Commercially Available Li-Ion Battery Electrode. *J. Electrochem. Soc.* **2012**, *159*, A1023−A1027.
(9) Ebner, M.; Marone, F.; Stampanoni, M.; Wood, V. Visualization and Quantification of Electrochemical and Mechanical Degradation in Li Ion Batteries. *Science* **2013**, *342*, 716−721.
(10) Moroni, R.; Börner, M.; Zielke, L.; Schroeder, M.; Nowak, S.; Winter, M.; Manke, I.; Zengerle, R.; Thiele, S. Multi-Scale Correlative Tomography of a Li-Ion Battery Composite Cathode. *Sci. Rep.* **2016**, *6*, 30109.
(11) Zielke, L.; Hutzenlaub, T.; Wheeler, D. R.; Manke, I.; Arlt, T.; Paust, N.; Zengerle, R.; Thiele, S. A Combination of X-Ray Tomography and Carbon Binder Modeling: Reconstructing the Three Phases of LiCoO2 Li-Ion Battery Cathodes. *Adv. Energy Mater.* **2014**, *4*, 1301617.
(12) Komini Babu, S.; Mohamed, A. I.; Whitacre, J. F.; Litster, S. Multiple Imaging Mode X-Ray Computed Tomography for Distinguishing Active and Inactive Phases in Lithium-Ion Battery Cathodes. *J. Power Sources* **2015**, *283*, 314−319.
(13) Morelly, S. L.; Tang, M. H.; Alvarez, N. J. The Impotence of Non-Brownian Particles on the Gel Transition of Colloidal Suspensions. *Polymers* **2017**, *9*, 461.
(14) Morelly, S. L.; Alvarez, N. J.; Tang, M. H. Short-Range Contacts Govern the Performance of Industry-Relevant Battery Cathodes. *J. Power Sources* **2018**, *387*, 49−56.
(15) Tkachuk, A.; Duewer, F.; Cui, H.; Feser, M.; Wang, S.; Yun, W. X-ray Computed Tomography in Zernike Phase Contrast Mode at 8 keV with 50-Nm Resolution Using Cu Rotating Anode X-ray Source. *Z. Kristallogr. - Cryst. Mater.* **2007**, *222*, 650−655.
(16) Merkle, A. P.; Gelb, J. The Ascent of 3D X-Ray Microscopy in the Laboratory. *Microsc. Today* **2013**, *21*, 10−15.
(17) Ebner, M.; Chung, D. W.; García, R. E.; Wood, V. Tortuosity Anisotropy in Lithium-Ion Battery Electrodes. *Adv. Energy Mater.* **2014**, *4*, 1301278.
(18) Mendoza, H.; Roberts, S. A.; Brunini, V. E.; Grillet, A. M. Mechanical and Electrochemical Response of a LiCoO2Cathode Using Reconstructed Microstructures. *Electrochim. Acta* **2016**, *190*, 1−15.
(19) Rahani, E. K.; Shenoy, V. B. Role of Plastic Deformation of Binder on Stress Evolution during Charging and Discharging in Lithium-Ion Battery Negative Electrodes. *J. Electrochem. Soc.* **2013**, *160*, A1153−A1162.
(20) Stephenson, D. E.; Hartman, E. M.; Harb, J. N.; Wheeler, D. R. Modeling of Particle-Particle Interactions in Porous Cathodes for Lithium-Ion Batteries. *J. Electrochem. Soc.* **2007**, *154*, A1146.
(21) Bauer, W.; Nötzel, D.; Wenzel, V.; Nirschl, H. Influence of Dry Mixing and Distribution of Conductive Additives in Cathodes for Lithium Ion Batteries. *J. Power Sources* **2015**, *288*, 359−367.
(22) Besnard, N.; Etiemble, A.; Douillard, T.; Dubrunfaut, O.; Tran-Van, P.; Gautier, L.; Franger, S.; Badot, J.-C.; Maire, E.; Lestriez, B. Multiscale Morphological and Electrical Characterization of Charge Transport Limitations to the Power Performance of Positive Electrode Blends for Lithium-Ion Batteries. *Adv. Energy Mater.* **2017**, *7*, 1602239.
(23) Garboczi, E. J.; Bentz, D. P.; Martys, N. S. Digital Images and Computer Modeling. *Experimental methods in the physical sciences*; Elsevier, 1999; Vol. 35, Chapter 1, pp 1−41, DOI: 10.1016/S0076-695X(08)60412-3.
(24) Harris, S. J.; Lu, P. Effects of Inhomogeneities—Nanoscale to Mesoscale—on the Durability of Li-Ion Batteries. *J. Phys. Chem. C* **2013**, *117*, 6481−6492.
(25) Jaiser, S.; Funk, L.; Baunach, M.; Scharfer, P.; Schabel, W. Experimental Investigation into Battery Electrode Surfaces: The Distribution of Liquid at the Surface and the Emptying of Pores during Drying. *J. Colloid Interface Sci.* **2017**, *494*, 22−31.
(26) Lim, S.; Ahn, K. H.; Yamamura, M. Latex Migration in Battery Slurries during Drying. *Langmuir* **2013**, *29*, 8233−8244.
(27) Hagiwara, H.; Suszynski, W. J.; Francis, L. F. A Raman Spectroscopic Method to Find Binder Distribution in Electrodes during Drying. *J. Coatings Technol. Res.* **2014**, *11*, 11−17.
(28) Jaiser, S.; Müller, M.; Baunach, M.; Bauer, W.; Scharfer, P.; Schabel, W. Investigation of Film Solidification and Binder Migration during Drying of Li-Ion Battery Anodes. *J. Power Sources* **2016**, *318*, 210−219.
(29) Müller, M.; Pfaffmann, L.; Jaiser, S.; Baunach, M.; Trouillet, V.; Scheiba, F.; Scharfer, P.; Schabel, W.; Bauer, W. Investigation of Binder Distribution in Graphite Anodes for Lithium-Ion Batteries. *J. Power Sources* **2017**, *340*, 1−5.

DOI: 10.1021/acsaem.8b01184
ACS Appl. Energy Mater. XXXX, XXX, XXX−XXX